WHIRL FLUTTER ANALYSIS OF A TILTROTOR SEMI-SPAN WIND TUNNEL MODEL FOR TEST RESULTS CORRELATION

Juan Montaño-Oliveros, Leonardo Helicopters, Cascina Costa, Italy
Federico Fonte, Leonardo Helicopters, Cascina Costa, Italy
Stefan van ‘t Hoff, Royal Netherlands Aerospace Centre (NLR), Amsterdam, Noord-Holland, Netherlands
Bart Timmerman, Royal Netherlands Aerospace Centre (NLR), Amsterdam, Noord-Holland, Netherlands

Abstract

The Clean Sky 2 Advanced Testbed for TILtrotor Aeroelastics (ATTILA) project is aimed at whirl flutter testing of a semi-span wind tunnel model of a tiltrotor, and is intended to support the development of the Next Generation Civil Tiltrotor (NGCTR) Technology Demonstrator. The wind tunnel model has been designed by targeting the main dynamic properties of the full scale demonstrator, and multiple analytical models were used and cross-validated to drive the design choices. The main model components were dynamically characterized after manufacturing with the double aim of checking the design and to correlate the numerical models. This paper provides an overview of the wind tunnel model and describes the numerical models used to predict its whirl flutter characteristics. It also presents the correlation of the numerical models based on the experimental data. Finally, sensitivity analyses are presented that allows both to identify the most relevant parameters affecting whirl flutter, and to quantify the impact that uncertainty on model parameters can introduce in the frequency and damping of the main whirl flutter modes.

1. NOMENCLATURE

Symbols

ω	Damped frequency, rad/s
ω_{WB}	Natural frequency of the first wing beam bending mode

Acronyms

QC	Quarter Chord
TD	Technology Demonstrator
CFD	Computational Fluid Dynamics
CG	Center of Gravity
DS	Downstop
FEM	Finite Element Model
FOSS	Fiber Optic Sensor System
FRF	Frequency Response Function
GVT	Ground Vibration Tests
IADP	Innovative Aircraft Demonstrator Platform
LHD	Leonardo Helicopters
MAC	Modal Assurance Criterion
NGCTR	Next Generation Civil Tiltrotor
NR	Number of Rotations
NSM	Non Structural Masses
OAT	Outside Air Temperature
P	Progressive
QC	Quarter Chord
R	Regressive
RDAS	Rotating Data Acquisition System
TD	Technology Demonstrator
WB	Wing Beam (out-of-plane) bending mode
WC	Wing Chord (in-plane) bending mode
WT	Wing Torsion mode

2. INTRODUCTION

The interest in tiltrotor technology has been increasing in the last decades, thanks to its capability to provide higher forward speeds than helicopters while retaining vertical take-off capability and ensuring high endurance (Ref 1). For this reason, a Next Generation Civil Tilt Rotor Technology Demonstrator (NGCTR-TD) is currently under development by Leonardo Helicopters Division (LHD) as one of the two Integrated Aircrafts Technology Demonstrators foreseen by the Horizon 2020 Clean Sky 2 Fast Rotorcraft IADP (Innovative Aircraft Demonstrator Platform) funding framework.

The tiltrotor configuration offers a high level of operational capabilities, but the complexity of the configuration implies that aeroelastic phenomena can introduce limitations in the design and in the operative envelope. In particular, high-speed aeroelastic instability involving both the proprotor and airframe, known as whirl flutter, can represent a major limitation of the flight envelope (Refs. 2-4). There is then need to move the limitation introduced by whirl flutter further away from the flight envelope and to do so in an efficient way, to avoid introducing penalizations in the aircraft performances. It is then important to accurately predict it so to properly address the aircraft design. With that aim, experimental characterization and wind tunnel tests are important tools that can be used to increase the understanding of the whirl flutter instability and to improve the confidence in the numerical models, and several wind tunnel aeroelastic tests campaigns have been conducted over the years. The JVX model was designed and tested in the 1980s to support the development of the V22 aircraft (Ref. 6), and was later further developed into the Wing and Rotor Aeroelastic Test System (WRTAS) (Ref. 7). The ADYN tests performed in the DNW Large Low-speed Facility (Ref. 8) investigated the whirl flutter characteristics of the ERICA concept (Ref. 9). The development of wind tunnel models for whirl flutter characterization is still an active research branch and the Maryland Tiltrotor Rig is currently under development at the University of Maryland (Ref.10). NASA and US Army developed the TiltRotor Aeroelastic Stability Testbed (TRAST) (Refs. 11, 12) which recently underwent wind tunnel testing (Ref. 13). Also the development of the NGCTR-TD is supported by a wind tunnel experimental characterization of the whirl flutter behaviour, and this activity is being conducted under the Clean Sky 2 ATTILA project.

The goal of the ATTILA project is to perform whirl flutter wind tunnel tests of a cantilevered tiltrotor wing equipped with a powered proprotor. The model is designed to replicate the relevant dynamics characteristics of the NGCTR-TD and the test results will be used both to check the aircraft configuration as well as the accuracy of numerical prediction tools. To this end, the test envelope will cover high-speed forward flight conditions, considering both power-on and power-off conditions.

The complex setup required for the above-described wind tunnel tests needs to be accurately characterized during its design to ensure that the target dynamic characteristics will be matched by the test model. Further experimental characterization is required once the design is complete in view of the actual wind tunnel test configuration, leading to the determination of the expected frequency and damping of the main aeroelastic modes. The dynamic response predictions performed after the model design can benefit from the experimental characterization performed on the manufactured components and assemblies, enabling the predictions of the numerical analysis to form the basis for the definition of the test matrix. The numerical results also constitute a reference that is useful to identify anomalies during test. In order to constitute an effective reference, the numerical results must take into account also the variation of key model parameters that can follow from operational variability, from possible mismatch between the numerical model properties and the physical properties of the test setup, and from the inaccuracies of the numerical models. It is then possible to generate confidence regions where the experimental damping and frequencies are expected to be found.

The present paper describes the definition of the numerical aeroelastic models that are being used in preparation for the tests, as discussed above. The definition of the model will be described including the comparison with experimental results available, and the stability results in the test envelope will be presented. Finally, the key uncertain parameters affecting the response will be identified and their impact on frequency and damping of whirl flutter modes will be presented.

3. ATTILA TESTBED

The ATTILA wind tunnel testbed has been designed as a Mach-scale cantilever half-wing representation of the NGCTR. The ATTILA testbed shown in Figure 1 features a stiff in-plane 1.25 m (4.1 ft) radius three-bladed constant-velocity gimballed rotor with flexured hub, mounted on a 1.8 m (5.9 ft) semi-span wing. The rotor is powered by a water-cooled 17.5 kW (23.5 hp) brushless DC electric motor situated in the tiltable part of the nacelle, obviating the need for a through-wing driveshaft and split 90-degrees gearbox. The wing root is directly cantilevered to the test section floor/wall and consists of an aeroelastically tailored rectangular carbon fiber beam, eight structurally isolated airfoil segments, and numerous adjustable non-structural masses (NSM).

The wing-nacelle bracket features a decoupled six-component load balance that measures all aerodynamic loads except for those on the nacelle fairing. Rotor torque is measured by an instrumented flex-coupling installed in front of the gearbox. Redundant measurement of the in-plane hub forces is provided by strain instrumentation on the rotor mast. Beyond the load measurement capability, the torque flex-coupling and rotor load balance are primary design elements for tailoring the structural dynamics of the wing-pylon and drive train to match the full-scale reference.

A remote-control downstop locking mechanism and parallel actuator spring restrain pylon tilt and enable in-situ pylon pitch and yaw stiffness tuning independently for the on-downstop and off-downstop configurations. To achieve pure wind milling operation, a retractable collar is mounted to the motor output shaft that enables decoupling the motor. The proprotor blades are constructed from ultrathin-ply glass fiber fabric (0.045 mm) with a foam core and incorporate both conventional strain gauges and fiber optic sensors integrated in the D-spar for load measurement, safety of flight monitoring, and dynamic characterization. The same thin-ply glass laminate is also used for the yoke which provides the flexural flap and lag articulations and the physical interface for blade retention through a set of pitch-change bearings. The blade consists of a load-carrying D-spar structure at the front and a thin co-bonded airfoil section behind the D-spar. The D-spar geometry and composite layup has been tailored to replicate the target radial distribution of the blade elastic properties, aiming to match the target frequencies and mode shapes of at least the first five isolated blade modes. The inside of the D-spar is filled with a foam core to offer geometrical stability and prevent buckling of the (very) thin load-carrying laminates.

The outboard bearing assembly isolates the yoke from flap and lag bending moments through a universal joint located at the radial station of the blade attachment pins and reacts the centrifugal loads via a set of three aerospace series spherical ball bearings. The inboard bearing assembly restrains flap and lag displacement, enabling free rotation and axial displacement at the blade root. Proprotor blade pitch control is achieved through a cyclic swashplate below the rotor and a rise-and-fall collective head assembly inside the spinner. The collective head is mounted on a rotating collective tube that extends through the drive shaft and gearbox and is translated by a lever attached to the housing of the annular digital slip ring. Translation of the collective head produces a collective blade pitch control input through a collective lever mechanism attached to the blade pitch links and the cyclic swashplate links.

Independent trim-excitation units mounted on the tiltable pylon provide full-range trim pitch control and 0-25 Hz variable-amplitude sinusoidal flutter excitation inputs on all three control axes (collective, cyclic lateral and cyclic longitudinal proprotor pitch). The system enables ramped amplitude excitation with rapid cut-off for free decay measurements and for use in case an excessive system response is observed.

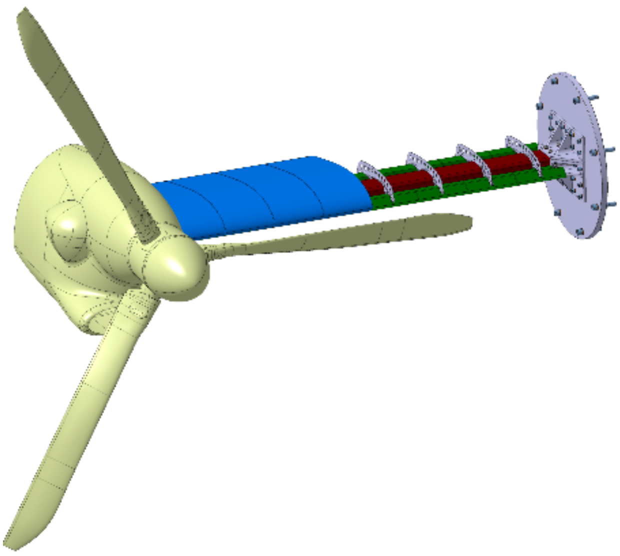

Figure 1: ATTILA testbed

4. NUMERICAL AEROELASTIC MODEL

Three different numerical models of the ATTILA testbed have been set up: a FLIGHTLAB (Ref. 14) model developed by NLR, a CAMRADII (Ref. 15) model developed by LHD, and finally an MBDyn (Ref. 16) model developed by Politecnico di Milano. Having different codes is useful at this stage to explore the use of different levels of approximation for the modeling of the aeroelastic response, and to provide a cross-validation of the models prior to comparison with experimental data.

4.1. CamradII model

The ATTILA CAMRADII model contains all the elements required for a representative description of the fundamental dynamics of the testbed. The complexity of the control chain, shaft and drive train mechanisms is not modelled to the detail for each single component, but approximated to a significant set of bodies with the necessary inertia and kinematic properties.

The aeroelastic model is formed by three blades composed of beam finite elements, connected to the shaft by the three arms of the yoke (again made of beam finite elements). The geometry, inertia and stiffness properties of the blades and yoke are defined in terms of 1D distributions obtained from FEM analysis and tuned to match experimental measurements as will be described in section 5.1.

The blade and yoke are connected by two bearings (inner and outer). The inner bearing at the blade root constrains the chord and normal relative displacements, but is free in the rotations and axial displacement. The outer bearing is modelled by a series of rotating and linear springs. The outer bearing rotational stiffness is very low so it actually works as a pinned interface. The yoke is connected to the shaft by a gimballed joint that guarantees a constant velocity of the rotor.

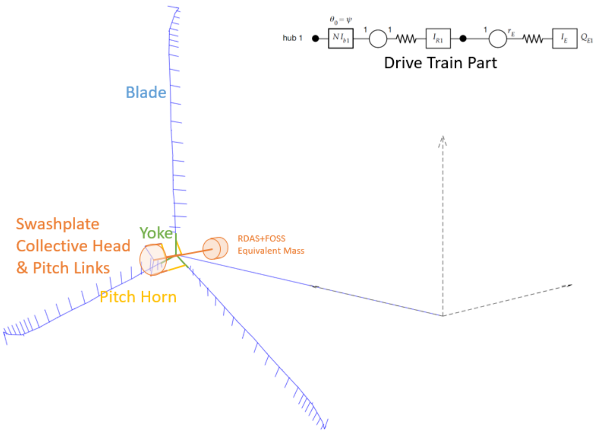

Figure 2: CAMRDADII model overview

The ATTILA wind tunnel model control chain is very complex. However, it is possible to define simplified models with increasing levels of complexity to determine the effect of control chain modeling on the fundamental dynamics of the rotor and its influence on the whirl flutter predictions. As a first approximation, the CAMRADII model includes a set of pitch links connected to the blade by a rigid pitch horn and a tilting solid disk, capable of moving along the rotor shaft. The tilt of the swashplate controls the cyclic angle of the blade, whereas the displacement along the shaft defines the collective angle. The solid disk has a mass and inertia associated with it.

Although the control chain kinematics can be captured by this model, the mass distribution requires further modifications. The ATTILA control chain includes a significant mass on the aft end of the shaft (the RDAS and FOSS) that moves axially following a change of collective pitch. This mass has an important effect on the nacelle center of gravity and inertia and, therefore, on the airframe and rotor modes interaction. For this reason, the CAMRADII model includes a dedicated definition of these masses that allows to consider the proper variation of the system center of mass.

The rotor is connected to the airframe and drive train parts. The first four airframe modes (wing beam, chord, torsion and pylon yaw) have been considered in the whirl flutter analysis. The airframe modes are inserted in the linearized rotor model as normal linear modes applied to the swashplate and hub; they include the effect of down-stop and pylon stiffness. The non-linear trim analysis considers a fixed rotor position, hence a rigid airframe. A simplified one degree of freedom drive train is connected to both the hub and the swashplate, providing a constant rotor speed. The rotor speed perturbation is enabled during the stability calculations.

The aerodynamic forces on the blade are calculated by iterative methods, the final circulation distribution along the blade must be coherent with the induced inflow produced by the wake. Considering the high-speed airplane mode conditions to be tested, a prescribed rigid wake (a pure helicoidal) can provide an appropriate approximation of the inflow analysis during the non-linear trim task. The inflow variations during the linear stability analysis are modelled by dynamic inflow. The inflow map together with the blade kinematics provide an angle of attack distribution along the blade that enables the aerodynamic coefficient calculation via look-up table (c81 tables). The aerodynamic coefficients have been obtained by CFD simulation by NLR.

4.2. FLIGHTLAB Model

In contrast to the modal approach employed in CAMRADII, the FLIGHTLAB the wing and pylon are modelled using non-linear beam elements the formulation of which employs slender flexible beam assumptions. Concentrated mass components represent the airfoil segments, nacelle fairings and the other nonstructural wing and nacelle parts. In nominal configuration, the wing beam is rigidly cantilevered, which approximates the true interface. An alternative model is available in which spring restraints at the wing root represent the equivalent stiffness of the wing root bracket attachment. The load balance situated between the wing beam and pylon is represented by a series connection of three translational springs, followed by three rotational springs. The balance is connected to the controllable pylon tilt hinge which, in turn, is connected on the child side to the downstop gimbal spring that represents the stiffness of the downstop mechanism. The pitch and yaw stiffness of the gimbal spring that represents the downstop can be changed at run-time to switch between the on-downstop and off-downstop configurations. The mass of the RDAS is attached to the pylon through a controlled slider that translates with collective pitch.

The rotor assembly model consists of the yoke, three blades and the control chain. The yoke and blade are represented by means of the same nonlinear beam elements as used for the wing. The blade elastic axis is staggered in the local chordwise direction and swept near the tip to approximate the radial locus of shear centers. The aerodynamics of the blade are modelled by means of table look-up with a correction for unsteady circulatory effects and the aforementioned Reynolds number effects. The rotor inflow modelling depends on the application, but in most cases an unsteady uniform inflow model was used, neglecting interactional effects.

The latest iteration of the rotor model also accounts for airfoil non-circulatory effects, a feature not available in the current FLIGHTLAB release. The capability was achieved by adopting the necessary parts of the ONERA dynamic stall model and combining these with the default unsteady aerodynamics model. The non-circulatory aerodynamics has a significant effect on the predicted damping of the rotor modes, particularly for those modes that are dominated by pitch. Although the impact on the whirl flutter predictions is minimal, the addition meant the distinction between a stable and unstable rotor in over-speed conditions.

The blade is connected to the yoke in two locations, at the inner bearing and at the outer bearing. To facilitate the dual load path introduced by the combination of the blade and the yoke, the root-end of the blade is modelled as a separate beam that is inverted, starting at the outer bearing, and connected at the physical root via the inner bearing. The inner bearing is represented using a zero-length 2-parent translational spring of practically infinite stiffness, combined with a zero-length zero-stiffness 1-parent axial spring. The 2-parent translational spring has no inherent orientation and, therefore, restricts translational movement in all directions. The axial spring, connected in series with the translational springs, allows unrestrained movement in the local axial direction of the deformed yoke.

The outer bearing is modelled as a series of three one-dimensional torsional springs with zero spring stiffness, allowing rotation around all three axes while constraining translation. In accordance with the design, the pitch articulation is radially displaced from the collocated flap/lag hinges that represent the outer universal joint.

To correctly capture the mass and inertia of the hub, pitch horn and pitch change bearings, associated concentrated mass elements have been defined and connected in their appropriate frames of reference. An additional mass is attached to the hub and is used to align the total rotor assembly mass and center of gravity with that of the NASTRAN structural dynamics model. Its mass includes, e.g., the mass of the spinner and the constant-velocity joint. The position is determined based on the difference between the target rotor assembly center of gravity and the nominal position derived by FLIGHTLAB at model initialization.

The baseline pitch control chain model is similar to the one adopted in CAMRADII, but alternative formulations have been developed up to and including a full kinematic model of the complete split control chain. The stiffness properties of the control chain models in FLIGHTLAB were tuned to match a detailed 3-D NASTRAN model representing the full control chain. The stiffness was determined both in NASTRAN and FLIGHTLAB by consecutively applying collective and cyclic unit pitch loads at the inner bearings (under rigid blade and yoke assumptions) and deriving the stiffness matrix from the resulting pitch rotations expressed in multi-blade coordinates. The total mass in the collective chain was initially set equal to the rigid body mass of the pitch control system collective mode as obtained in NASTRAN. The mass has subsequently been scaled to match the frequency of the 1st collective mode as predicted by NASTRAN. The conventional swashplate model requires significantly more scaling than the full kinematic model. The cyclic inertia, which for the full kinematic model is distributed between the rockers and the cyclic swashplate, was directly tuned to the relevant modal frequency.

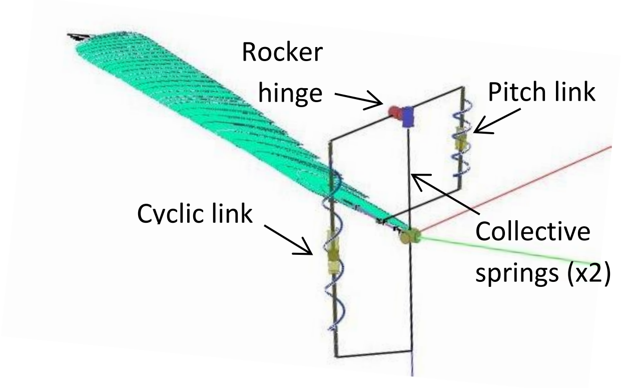

Figure 3: Visual representation of full kinematic pitch control chain model in FLIGHTLAB.

5. CHARACTERIZATION TESTS

5.1. Overview

To date, dynamic characterization testing of the ATTILA wind tunnel model has encompassed Ground Vibration Testing (GVT) of the:

- Load balance
- Yoke
- Blades
- Yoke-blade assembly
- Wing

Additional testing that is planned includes GVTs of the isolated pylon and the complete wing-pylon-rotor assembly, as well as stiffness measurements of the pitch control system and drive train.

5.2. Yoke

The yoke was tested in both free-free and fixed-free conditions. *Figure 4* shows the test set-up for the isolated yoke in free-free conditions with the yoke suspended with elastic rubber bands. A single uni-axial accelerometer was employed to minimize the impact of the mass associated with the sensor (~0.5 grams). This accelerometer is attached to one of the yoke legs as seen in the bottom left of the figure. The yoke is excited with a tap hammer at 36 different locations (12 locations on each leg of the yoke), and the Frequency Response Function (FRF) is determined. It is noted here that the uni-axial accelerometer only measures accelerations in the out-of-plane direction of the yoke, and the yoke is also only excited in this z-direction. Nevertheless, as all modes except for the rigid body yaw mode will contain some out-of-plane displacement, the set-up can be used to characterize all the modes of interest. Figure 5 and Table 1 present the resulting correlation between test and FEM. Especially considering the fact that the yoke is a thick solid laminate structure for which the through-thickness stiffness properties were estimated, the accuracy of the FEM prediction is quite satisfactory.

Figure 4: Free-free yoke GVT test set-up

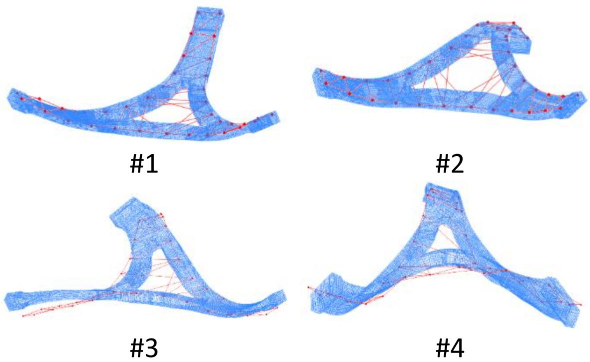

Figure 5: Mode shape correlation of the free-free yoke between GVT and FEM

Table 1: Correlation of dynamic properties of the free-free yoke between GVT and FEM

Mode	Frequency Error %	MAC
1	2.2	0.99
2	2.3	0.98
3	2.8	0.84
4	2.4	0.74
5	2.9	0.77
6	2.5	0.84

5.3. Blade

The blades were tested in free-free conditions, suspended in vertical orientation from bungees as shown in *Figure 6*. A tri-axial accelerometer was attached to the bottom (or pressure) side of the blade, while the blade was excited with a tap hammer from the top (or suction) side of the blade. *Table 2* presents the correlation between test and FEM considering the averaged test results for all four production blades. Blade-to-blade variations in frequency are less than 0.8%, indicating satisfactory repeatability in manufacturing. The correlation against FEM is reasonably good, though the expectations for a component with a sandwich-like structure were higher (~2%). The discrepancy may be attributable to the non-structural mass elements which are embedded inside the foam core of the blade. It is conceivable that, although not interconnected, these elements add a small amount of stiffness to the otherwise fairly flexible structure.

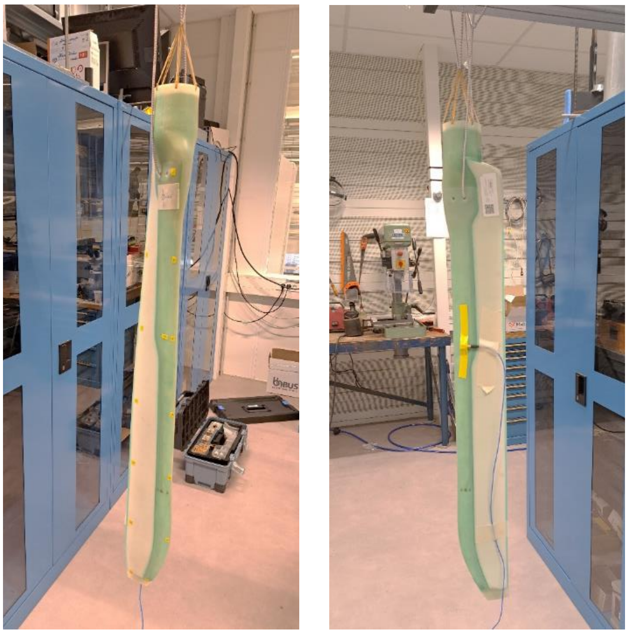

Figure 6: Free-free blade GVT test setup

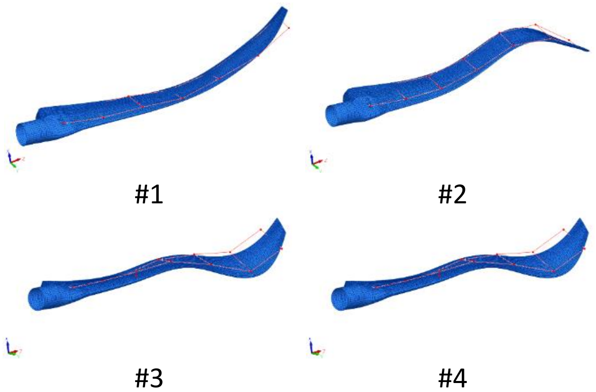

Figure 7: Mode shape correlation of the free-free blade between GVT and FEM

Table 2: Correlation of dynamic properties of the free-free blade between GVT and FEM

Mode	Frequency Error %	MAC
1	5.3	91.0
2	4.6	91.9
3	1.3	69.5
4	3.0	75.5
5	6.0	96.5

5.4. Yoke-blade assembly

In order to characterize the effect of the interface between the yoke and the blade, separate GVT tests were performed on the isolated yoke-blade assembly. *Figure 8* shows the set-up for the fixed-free tests where both the yoke and pitch link are rigidly clamped. The blade instrumentation is the same as used for the isolated blade GVT. Additional accelerometers were added to each leg of the yoke to confirm the rigid boundary condition of the yoke clamping. The correlation of the test results against numerical predictions was performed in CAMRADII and FLIGHTLAB and is presented in the next section.

Figure 8: Fixed-free yoke-blade assembly GVT test set-up

6. MODEL CORRELATION

The CAMADII rotor model consist on three blades mounted on a yoke structure, a simplified conventional swashplate control chain and a drive train model. The aeroelastic correlation has followed a step-by-step approach: each structural part has been separately created, checked against the dynamic characterization data, tuned (if required) and then assembled to the full rotor-wing model.

The free-free yoke has been modelled as three beams rigidly connected to a free hub center. This approach enables the correct representation of the first yoke modes, especially of those related to arm flapping.

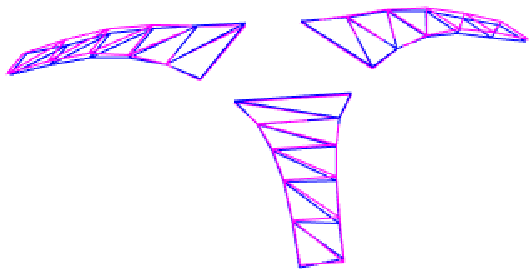

Figure 9: First yoke bending mode: comparison between numerical model (magenta) and experimental results (blue).

Only the high frequency modes (above 700 Hz) are explicitly affected by inter-arm dynamics so their impact in the comprehensive model is negligible. The low frequency ones show a good match in terms of modal shapes and MAC (>0.96), so no tuning on the provided property distributions has been carried out.

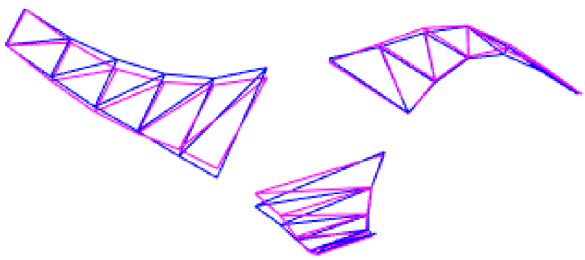

Figure 10: Second yoke bending mode: comparison between numerical model (magenta) and experimental results (blue).

The free-free single blade analysis has required further tuning: the provided mass and center of gravity distributions have been modified by the addition of linear corrections in order to reproduce the measured values of mass and center of mass location.

The flap, lag and torsion stiffness distributions have been divided in two zones (root and outboard blade) with a linear transition. A different tuning factor has been applied to each zone following a Newton-Raphson based iterative approach until target frequencies and MAC have been reached.

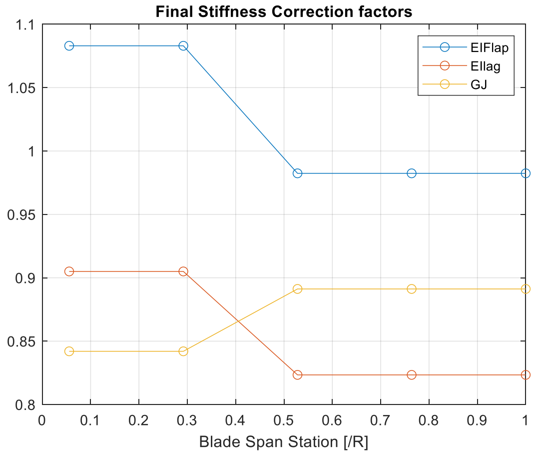

Figure 11: Correction factors applied to blade structural properties

The final correlation of the free-free blade shows a very good agreement with the experimental results.

Table 3: Correlation of dynamic properties of the free-free blade

Mode	Frequency Error %	MAC
1	0.19	0.91
2	-0.15	0.98
3	-0.65	0.87
4	-2.25	0.92
5	0.66	0.85
6	-1.74	0.93

The wind tunnel test blade was painted after dynamic characterization, so an extra distributed mass has been added to the final distribution in the whirl flutter simulations.

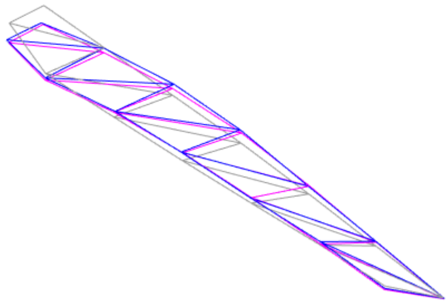

Figure 12: First blade mode shape, comparison between numerical model (magenta) and experimental results (blue).

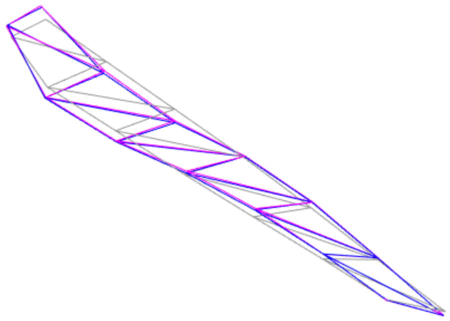

Figure 13: Second blade mode shape, comparison between numerical model (magenta) and experimental results (blue).

The yoke and blade have been separately correlated. Now it is possible to assemble both to a yoke-blade rotor and check it against the clamped rotor characterization test. In order to do so, the CAMRADII rotor model must be increased in complexity. No “shell” options are available to reproduce the characteristics of this rotor, so a heavy core modification is required. The rotor is originally set with a bearingless configuration, but then the core must be modified to accommodate the outer bearing. In this way, the outer bearing is modelled as pinned interface with three linear springs. The inboard bearing can be modelled by a snubber spring with zero axial stiffness.

Considering that the isolated blade and yoke have already been correlated, the free variables to tune in order to match the clamped rotor experimental modes are: the inboard normal springs, the outer normal springs, the outer axial spring and the pitch horn support flexibility.

The effect of these variables have been first checked by parameter sweeps. It shows a relatively narrow zone between saturation and exponential error were they can be tuned. Starting from this initial guess and in a similar fashion to the free-free blade correlation, a Newton-Raphson approach has been employed to reach the final tuning values.

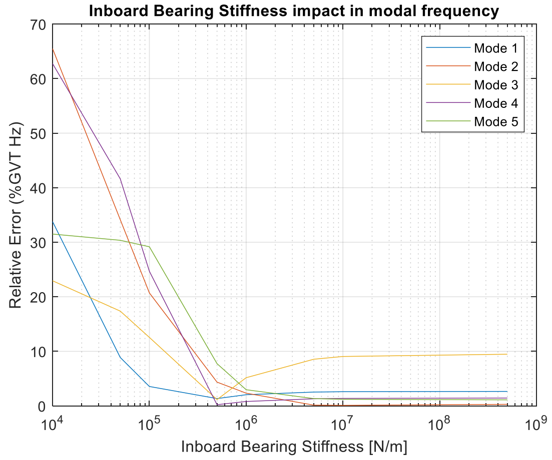

Figure 14: Impact of inboard bearing stiffness on error on mode frequency reconstruction

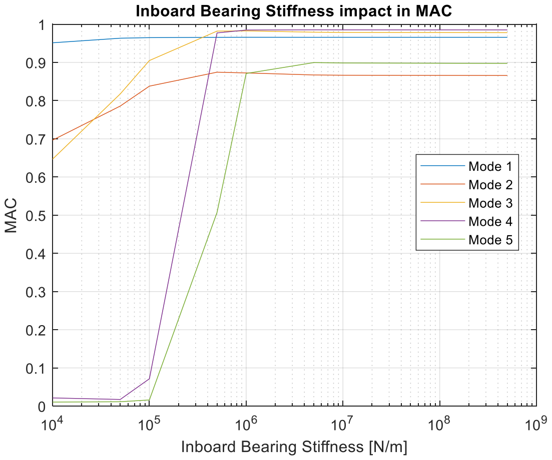

Figure 15: Impact of inboard bearing stiffness on error on modal MAC

The final correlation is satisfactory as all fundamental modes show similar deflection amplitudes and a very good match for frequencies and MAC.

Table 4: Correlation of dynamic properties of the yoke-blade system

Mode	Frequency Error %	MAC
1	2.03	0.97
2	-2.36	0.87
3	5.18	0.98
4	0.81	0.98
5	-2.96	0.87

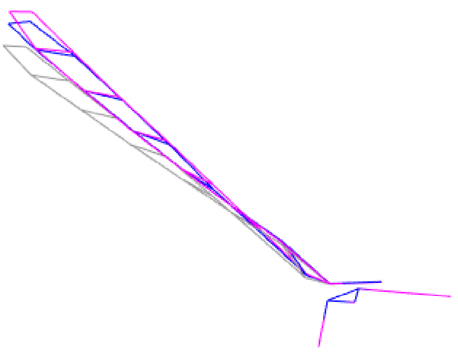

Figure 16: First mode of the blade+yoke assembly, comparison between numerical (magenta) and experimental (blue) mode shape.

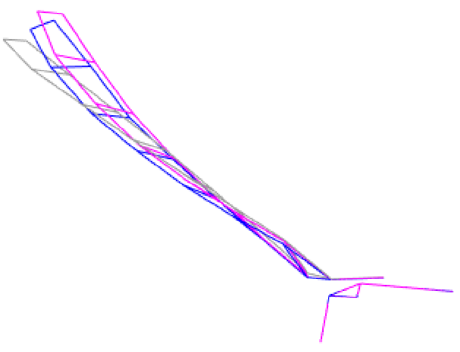

Figure 17: Second mode of the blade+yoke assembly, comparison between numerical (magenta) and experimental (blue) mode shape.

Figure 18: Third mode of the blade+yoke assembly, comparison between numerical (magenta) and experimental (blue) mode shape.

The in-vacuo fanplot obtained with the correlated model are shown in Figure 19 for the collective modes and in Figure 20 for the cyclic modes.

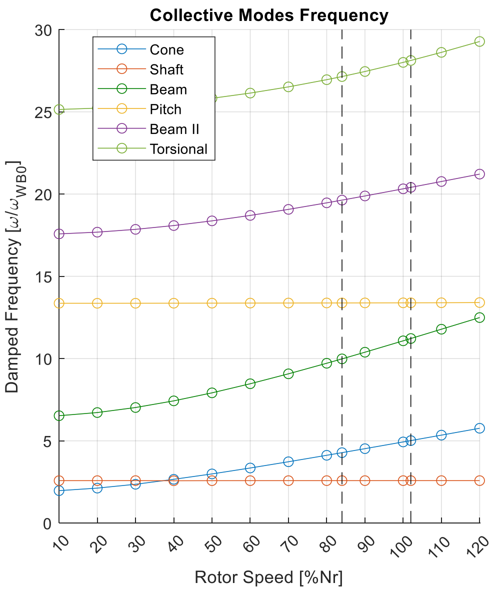

Figure 19: In vacuo fanplot: collective modes

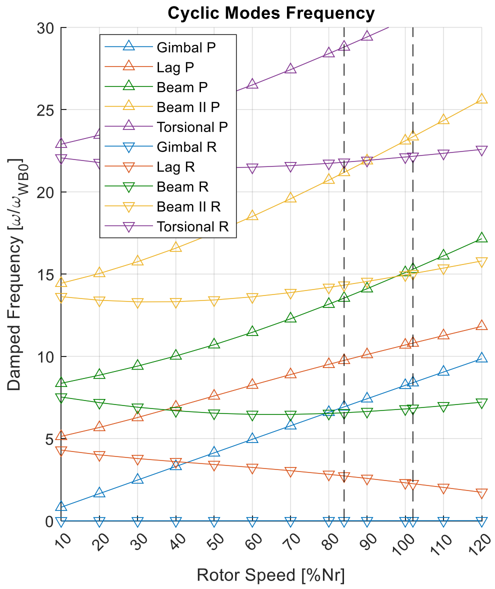

Figure 20: In vacuo fanplot: cyclic modes

7. WHIRL FLUTTER RESULTS

The numerical models are used to define the expected frequency and damping trends in the entire test envelope. The test envelope covers forward flight speed limited by either the wind tunnel limit or whirl flutter speed. The assessment is repeated by considering a variation

- In the rotor NR covering both the low NR of airplane mode flight configuration and the higher NR associated to VTOL flight conditions.
- Between power-on and power-off conditions.
- Between downstop-on and downstop-off conditions, that is by changing the pitch and yaw stiffness constraining the rotation of the pylon around the tilting axis.

The computed flutter trends are shown in Figure 21 and in Figure 22 power-ON and power-OFF conditions respectively. The critical mode visible in the figures is the wing torsion (WT) coupled with the rotor regressive gimbal mode.

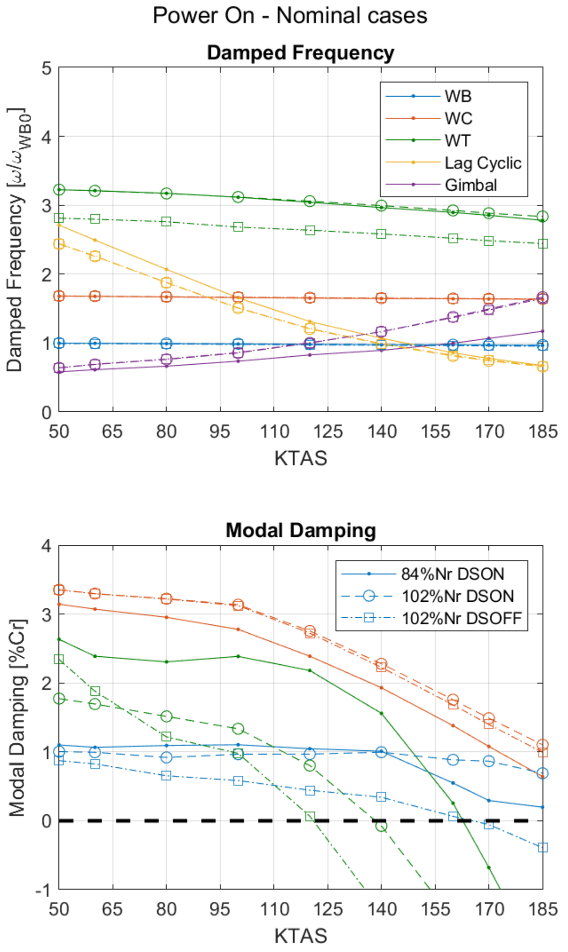

Figure 21: Frequency and damping of wing modes in Power ON conditions

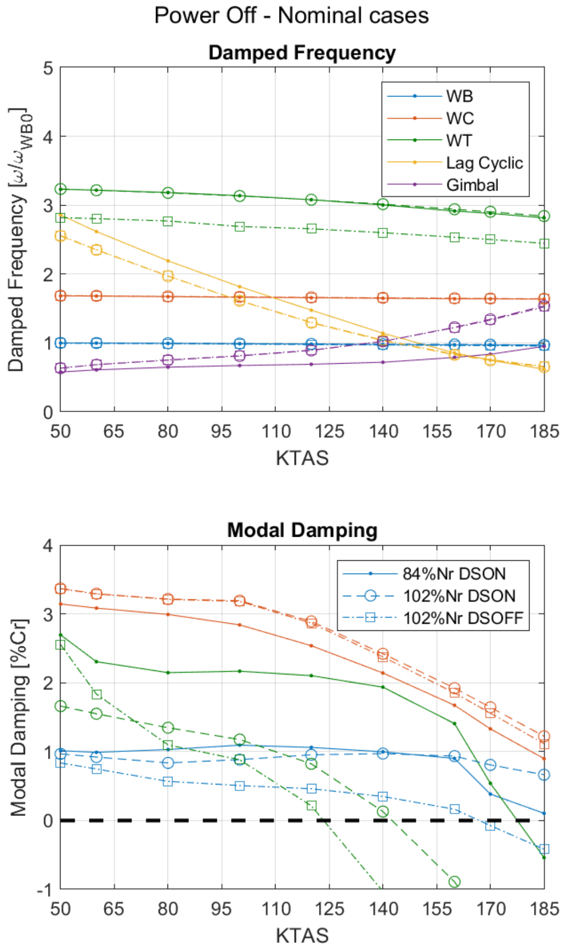

Figure 22: Frequency and damping of wing modes in Power OFF conditions

8. SENSITIVITY ANALYSIS

The numerical results described in the previous section are obtained with a nominal model operating in nominal conditions. To provide useful confidence regions for the frequency and damping estimates it is required to consider also the expected variation of the results following possible variation in operational condition (e.g. air temperature). It is also required to take into account the fact that the nominal model parameters (e.g. mass and stiffness distribution of the components) may not be fully representative of the actual setup. Finally, it is also possible that some difference exists between the numerical prediction and the experimental results due to the approximations introduced by the analytical modelling. While it is not possible to define a-priori all the previously listed variations, it is nonetheless useful to identify the main model parameters that are associated with them to enable the expected impact on the whirl flutter predictions to be determined.

The numerical results discussed above are completed with a sensitivity to some key parameters, namely

- Air temperature
- Blade Geometry
- Down-Stop and Mast Stiffness reduction
- Control Chain Stiffness Impact
- Blade Inertial Properties
- Blade Stiffness Distributions
- Bearing Stiffness
- Tip Loss Correction Settings.

The nominal cases already considered different NR, then provide an estimation of the impact of rotational speed on whirl flutter modes.

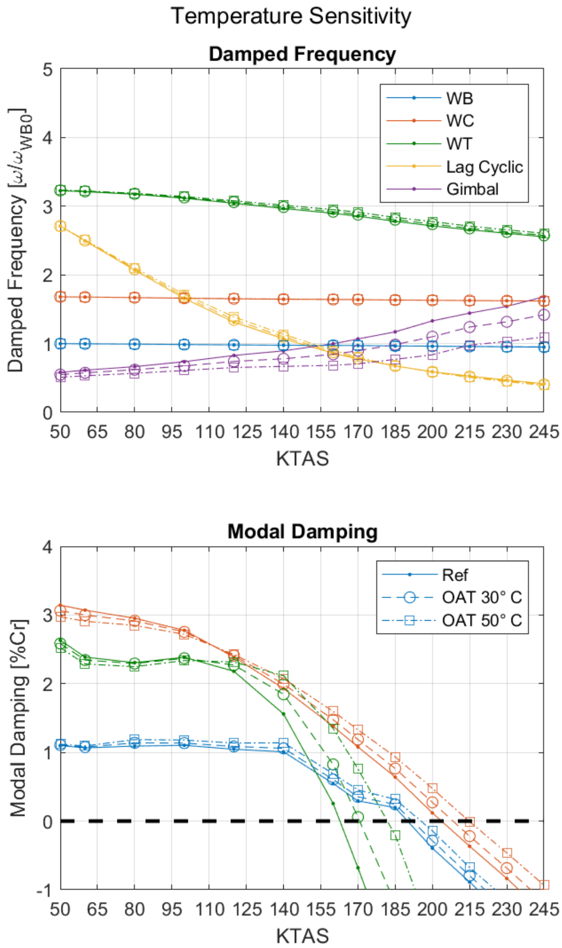

Figure 23: Temperature Effect Sensitivity

The operating condition has a large impact on whirl flutter characteristics, as shown in Figure 23. The increase in temperature (and associated density) results in an increase of flutter speeds. The baseline analyses were performed using standard day temperature, 30° C and 50° C have also been checked, with the aim of covering the full range that can be expected in the wind tunnel. The final comparison of numerical and experimental results will require the use of measured temperature to properly perform the numerical analyses.

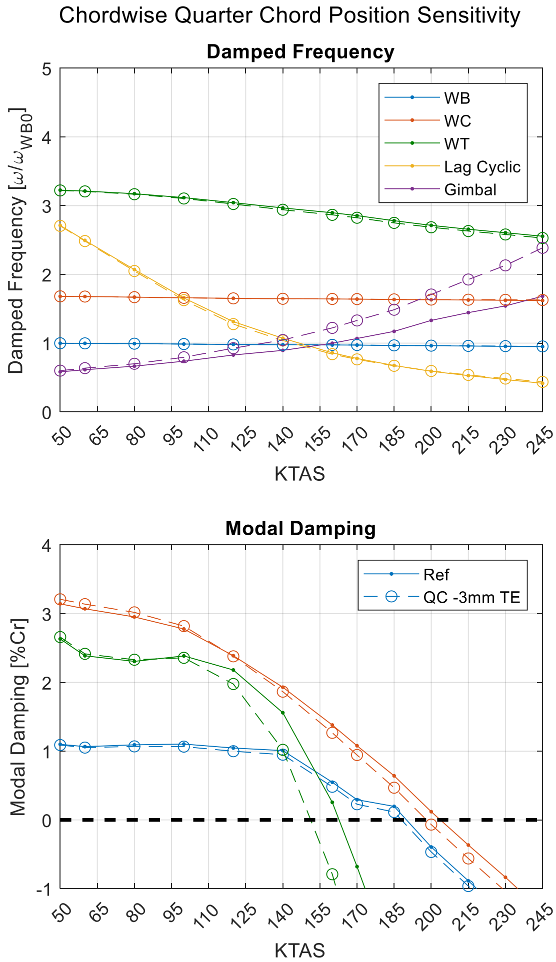

Figure 24: Blade Geometry Tolerances

Variations in blade geometry can also significantly impact whirl flutter characteristics. The effect of the expected errors in the quarter chord position have been calculated. It can be observed in Figure 24 that a 3 mm error on the tip (towards leading edge) has the effect of reducing the whirl flutter speed, whereas comparable errors in the dihedral angle do not show a significant influence. The chord positioning of the profiles has a large impact on the pitching moments and therefore on pitch-flap coupling, particularly if the distance to the local center of gravity is increased.

The effect on the gimbal mode is not negligible and the wing torsion mode damping decreases as the gimbal mode approaches it in terms of frequency.

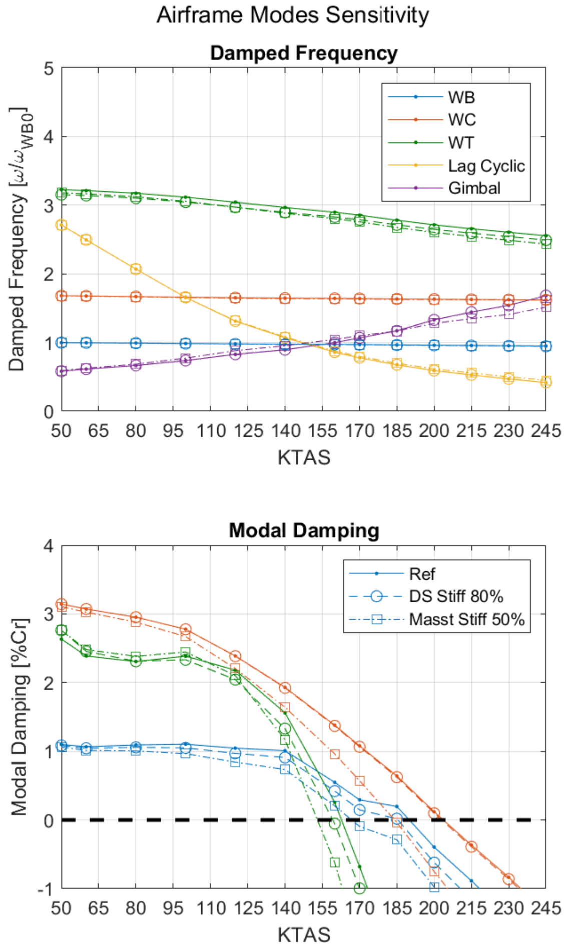

Figure 25: Airframe Modes Sensitivity

Errors on the Down-Stop and Mast stiffness (Figure 25) are possible due to manufacturing inaccuracies and non ideal connections. Any reduction in pylon stiffness has the consequence of reducing the flutter speed, as already noted by comparing the DS-ON and DS-OFF results in Figure 21.

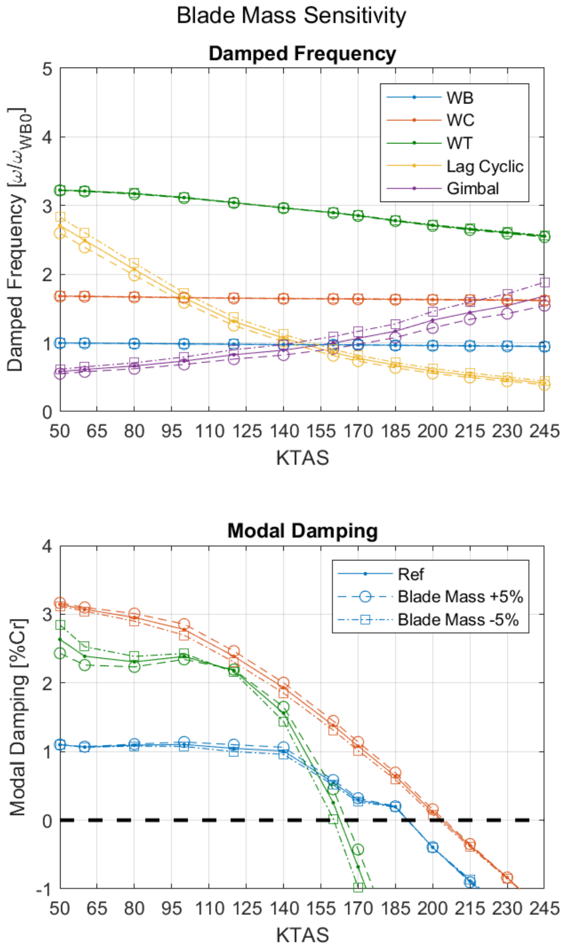

Figure 26: Mass Distribution Sensitivity

An increase in blade mass (Figure 26) has the double effect of increasing the total blade mass and of modifying the blade spanwise center of gravity location. Variations of blade mass, together with the local center of gravity (Figure 27) chordwise position are not negligible: both changes affect the gimbal mode frequency whose vicinity to the torsional mode influences the whirl flutter speed.

The cyclic regressive lag mode is almost unaffected by the sensitivities considered so far. Only the variation in mass distribution affected the cyclic lag mode frequency placement. Indeed, the most important parameters defining the cyclic lag mode frequency placement are the bearing stiffness (both the inner and outer bearings) as can be seen in Figure 28 and in Figure 29.

The lag cyclic mode has only a secondary impact on the definition of the damping trend of the whirl flutter modes. The ATTILA rotor shows much more sensitivity to perturbations affecting the gimbal mode and of course the isolated wing torsion mode.

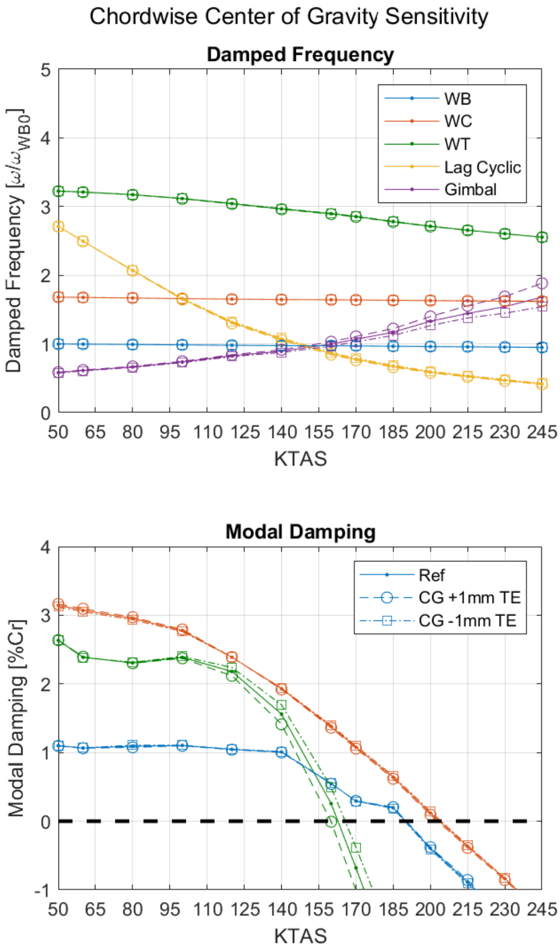

Figure 27: Sensitivity to blade chord-wise CG position

The flap, lag and torsional stiffness distributions along the blade have been analyzed with variations of up to 5% without significant impact. In the same way, the collective control chain stiffness has no influence on whirl flutter (though it is very important for the stability of the rotor system itself).

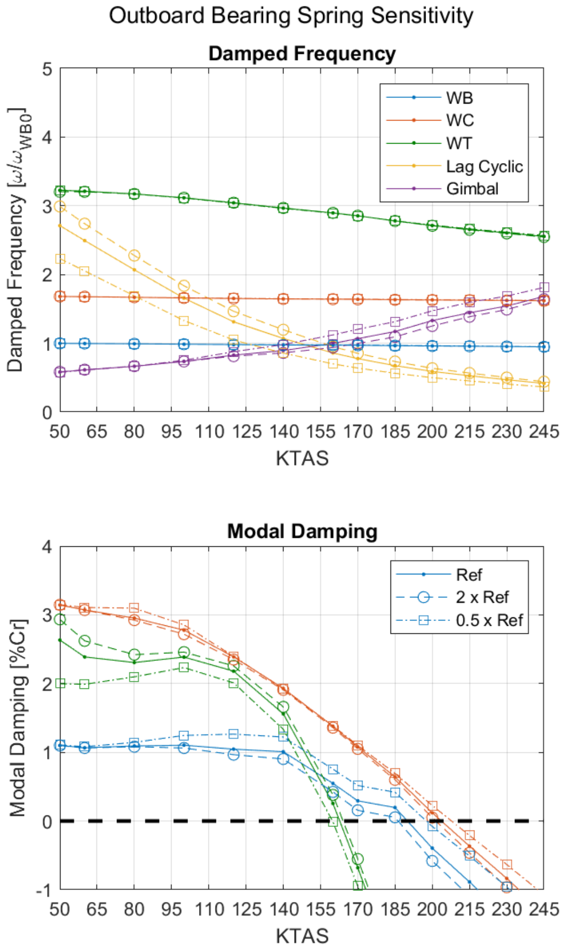

Figure 28: Sensitivity to equivalent inboard and outboard bearing stiffness

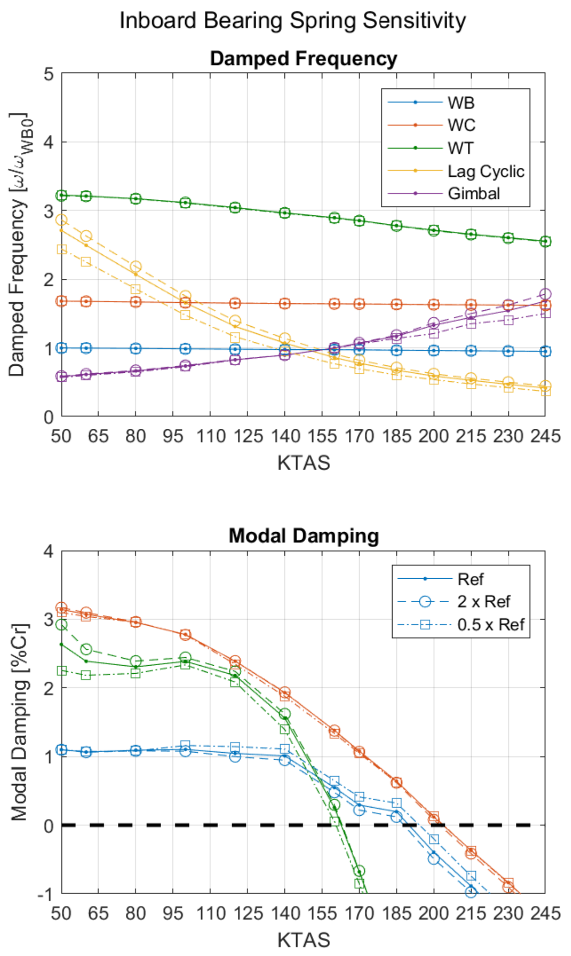

Figure 29: Sensitivity to equivalent inboard and outboard bearing stiffness

9. CONCLUSIONS

This paper discussed the ATTILA whirl flutter wind tunnel model along with two numerical models used to predict its aeroelastic characteristics defined respectively in CAMRADII and FLIGHTLAB. The correlation of the numerical models with the model components dynamic characterization test results was also discussed, showing that a good match between the numerical model and the experimental results can be obtained. The correlated models were then used to compute the frequency and damping of the main aeroelastic modes in all the nominal test conditions. The nominal analyses also served as the starting point for a sensitivity analysis covering expected uncertainty in operative conditions and in model definition. This sensitivity allowed the identification of the most relevant parameters in the definition of the whirl flutter characteristics. It also provides the data that will be used to generate confidence regions around nominal flutter trends where the actual frequencies and damping are expected to be found.

Author contact:

Juan Montaño-Oliveros, juan.montano-oliveros@leonardo.com,

Federico Fonte, federico.fonte@leonardo.com,

Stefan van ‘t Hoff, stefan.van.t.Hoff@nlr.nl,

Bart Timmerman, bart.Timmerman@nlr.nl

10. REFERENCES

1. Stevens, J., Rademaker, E., Scullion, C., Vouros, S., Nalianda, D., Pachidis, V., Van Oosten, N., Misté, G., Benini, E. and Venturelli, G., *Design Evaluation and Performance Assessment of Rotorcraft Technology by 2050*, 45th European Rotorcraft Forum, Warsaw, Poland, 2019.

2. Reed, W. H. III., *Review of Propeller-Rotor Whirl Flutter*, NASA/TR R-264, July 1967.

3. Johnson, W., *Dynamics of Tilting Proprotor Aircraft in Cruise Flight*, NASA Technical Note D-7677, May 1974.

4. Kvaternik, R., *An Experimental and Analytical Investigation of Proprotor Whirl-Flutter*, NASA Technical Paper 1047, December 1977.

5. Popelka, D., Sheffler, M., and Bilger, J., Correlation of Test and Analysis for the 1/5th-Scale V-22 Aeroelastic Model, Journal of the American Helicopter Society, April 1987 p. 21-33.

6. Settle, T. Ben, and David L. Kidd. *Evolution and Test History of the V-22 0.2-Scale Aeroelastic Model*. Journal of the American Helicopter Society 37.1 (1992): 31-45.

7. Piatak, David J.; Kvaternik, Raymond G.; Nixon, Mark W.; Langston, Chester W.; Singleton, Jeffrey D.; Bennett, Richard L.; and Brown, Ross K., A Wind-Tunnel Parametric Investigation of Tiltrotor Whirl-Flutter Stability Boundaries, 2003 International Forum on Aeroelasticity and Structural Dynamics, Amsterdam, The Netherlands, June 4-6, 2003.

8. Krüger, W. R., Multibody analysis of whirl flutter stability on a tiltrotor wind tunnel model, Proc. IMechE, Part K: J. of Multi-body Dynamics, Vol. 230, No. 2, 2016, pp. 121–133.

9. Nannoni, F., Giancamilli, G., and Cicalè, M., ERICA: the European Advanced Tiltrotor, 27th European Rotorcraft Forum, Moscow, Russia, 2001, pp. 55.1–15.

10. Datta, A., Tsai, F., and Sutherland-Foggio, J., Design of a New Tilt Rotor Test Facility at the University of Maryland, AIAA SciTech 2019 Forum, San Diego, CA, USA, 2019.

11. Kreshock, A.R., Kang, H., Yeo, H., and Acree, C.W., Development of a New Aeroelastic Tiltrotor Wind Tunnel Testbed, Annual AIAA SciTech Forum, San Diego, California, 2019.

12. Kreshock, A.R., Thornburgh, R.P. and Wilbur, M.L., Overview of the TiltRotor Aeroelastic Stability Testbed, Vertical AIAA SciTech Forum, San Diego, California, 2022.

13. Kreshock, A. R., Thornburgh, R. P., Wilbur, M. L., Kang, H., Piatak, D. J., & Sekula, M. K. Initial Whirl-Flutter Characterization of the TiltRotor Aeroelastic Stability Testbed. In Vertical Flight Society's 79th Annual Forum & Technology Display.

14. Du Val, R. W., and C. He. Validation of the FLIGHTLAB virtual engineering toolset. The Aeronautical Journal 122.1250 (2018): 519-555.

15. Wayne Johnson, Technology Drivers in the Development of CAMRAD II. Presented at the American Helicopter Society Aeromechanics Specialists Conference, San Francisco, California, January 19-21, 1994

16. P. Masarati, M. Morandini, P. Mantegazza An Efficient Formulation for General-Purpose Multibody/Multiphysics Analysis ASME J. Comput. Nonlinear Dyn., 9(4):041001, October 2014, doi:10.1115/1.4025628.